Intrinsic spin decay length in an antiferromagnetic insulator

Hiroto Sakimura,[1,2] Akio Asami,[2] Hiroki Hayashi,[2] Takashi Harumoto,[1] Yoshio Nakamura,[1] Ji Shi,[1] and Kazuya Ando[2,3,*]

[1]*School of Materials and Chemical Technology, Tokyo Institute of Technology, Tokyo 152-8552, Japan*
[2]*Department of Applied Physics and Physico-Informatics, Keio University, Yokohama 223-8522, Japan*
[3]*Center for Spintronics Research Network (CSRN), Keio University, Yokohama 223-8522, Japan*

We report intrinsic spin decay length of an antiferromagnetic insulator. We found that at an antiferromagnetic/ferromagnetic interface, a spin current generated by spin pumping is strongly suppressed by two-magnon scattering. By eliminating the two-magnon contribution, we discovered that the characteristic length of spin decay in polycrystalline NiO changes by two orders of magnitude through the paramagnetic to antiferromagnetic transition. The spin decay length in the antiferromagnetic state is around 100 nm, which is an order of magnitude longer than that previously believed. These results provide a crucial piece of information for the fundamental understanding of the physics of spin transport.

I. INTRODUCTION

Spintronics relies on the transport of spins in condensed matter [1–3]. Spin transport has been investigated in a variety of materials, including metals, semiconductors, and insulators. In metals and semiconductors, spins are transported by the diffusion of conduction electrons [3]. In contrast, in magnetically ordered materials, spins can be transported even in the absence of conduction electrons; spins are carried by the elementary excitations of magnetic moments, magnons [4]. The magnonic spin current in insulators is of particular recent interest because this sets a new direction for experimental and theoretical studies of the physics of spin transport [5,6].

Antiferromagnetic insulators is a new class of materials for spin transport [7–9]. This class of materials potentially entails a number of advantages as compared to ferromagnets; antiferromagnets are robust against external magnetic fields, produce no stray fields, and display ultrafast dynamics. Since the first observation of the transmission of spins through an antiferromagnetic insulator NiO [10–12], intense experimental and theoretical efforts have been invested in unraveling the physics of the spin transport in antiferromagnetic insulators [10–22]. Recent studies have shown that antiferromagnets allow long-distance spin transport [21,22]. However, the long spin decay length has been observed only in single crystals using nonlocal techniques; the spin decay length in amorphous or polycrystalline antiferromagnets is known to be limited to only a few nanometers [9].

In this paper, we demonstrate that the spin decay length of polycrystalline NiO, a prototypical antiferromagnetic insulator, is around 100 nm, which is an order of magnitude longer than that previously believed. We found that the spin decay length in NiO with columnar structure changes by two orders of magnitude through the paramagnetic to antiferromagnetic transition. These are evidenced by revealing the intrinsic character of magnonic spin transport by eliminating a two-magnon contribution in the spin-transmission signal. This result illustrates an essential role of the magnetic order in spin transport and shows the potential of polycrystalline antiferromagnetic insulators for good spin-current conductors.

II. METHODS

To quantify the intrinsic spin decay length of polycrystalline NiO, we prepared $Ni_{81}Fe_{19}(8)/NiO(d_{NiO})/Pt(5)$ trilayers on thermally oxidized Si substrates by rf magnetron sputtering at room temperature [see Fig. 1(a)]. The numbers in brackets represent the thickness of each layer in nm unit, where $d_{NiO} = 0$ to 10.5 nm. Here, the NiO layer is polycrystalline, which is evidenced by the x-ray diffractometry [23]. The $Ni_{81}Fe_{19}$ layer, capped by 4-nm-thick SiO_2, is a 1×1.5 mm^2 rectangular shape. For the $Ni_{81}Fe_{19}/NiO/Pt$ trilayers, we measured the spin pumping by varying a magnetic field **H** applied at an angle of θ_H from the film normal at room temperature [see Fig. 1(a)]. The spin pumping from the $Ni_{81}Fe_{19}$ layer injects a spin current into the NiO layer [24]. The spin current reaching the Pt layer is converted into an electric voltage V_{ISHE} through the inverse spin Hall effect (ISHE) in the Pt layer [25], and thus the spin-current decay in the NiO layer can be characterized by measuring the d_{NiO} dependence of V_{ISHE}. In Fig. 1(b), we show the H dependence of the microwave absorption intensity $I(H)$ and voltage $V(H)$ signals for the $Ni_{81}Fe_{19}/NiO/Pt$ trilayers with $d_{NiO} = 0$ and 4.1 nm at $\theta_H = 90°$. For the measurement, the $Ni_{81}Fe_{19}/NiO/Pt$ trilayer was placed at the center of a TE_{011} cavity with the frequency of $f = 9.43$ GHz and power of $P = 200$ mW, and we measured dc electric voltage V between

*Corresponding author should be addressed: ando@appi.keio.ac.jp
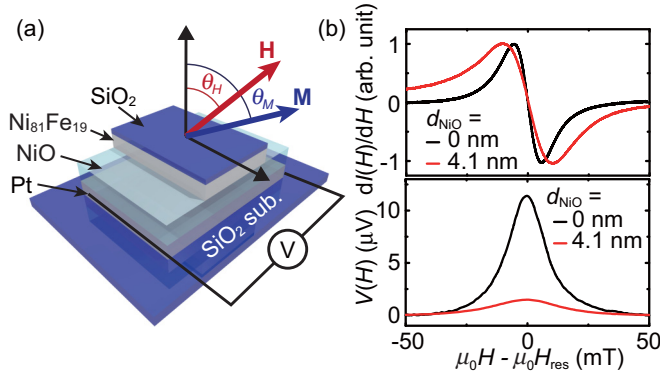
FIG. 1. (a) A schematic illustration of the $Ni_{81}Fe_{19}$/NiO/Pt tri-layer. **H** denotes the external magnetic field. **M** and θ_M represent the equilibrium direction of the magnetization when **H** is applied at an angle of θ_H from the film normal. (b) Magnetic field H dependence of the microwave absorption signal dI/dH and voltage signal V for the $Ni_{81}Fe_{19}$/NiO/Pt trilayers with $d_{NiO} = 0$ (black) and 4.1 nm (red). I is the microwave absorption intensity and H_{res} is the FMR field.

electrodes attached to the edges of the film [see Fig. 1(a)]. Figure 1(b) shows that the ISHE voltage V_{ISHE} is generated around the FMR field $H = H_{res}$. This result also shows that $V_{ISHE} \equiv V(H_{res})$ is strongly suppressed by inserting the NiO layer, as expected for the spin-current decay in the antiferro-magnet.

III. RESULTS AND DISCUSSION

Our finding is that magnetic-field angle θ_H dependence of V_{ISHE} strongly depends on the NiO thickness d_{NiO}. In Fig. 2(a), we show the θ_H dependence of V_{ISHE} for the $Ni_{81}Fe_{19}$/NiO/Pt trilayers with various d_{NiO}. This result shows that the θ_H dependence of V_{ISHE} for the trilayers with different d_{NiO} is the same only around $\theta_H = 0$. Here, the variation of V_{ISHE} for the film with $d_{NiO} = 0$ nm is consistent with the standard model of the spin pumping and ISHE [26]. In this model, when the magnetic damping constant α is independent of θ_H, the spin

current generated by the spin pumping is expressed as [26]

$$j_s(\theta_M) = \frac{g_{eff}^{\uparrow\downarrow} h^2 \hbar \gamma^2 \omega}{4\pi \alpha^2 A(\theta_M)[(4\pi M_s)^2 \gamma^2 \sin^4 \theta_M + 4\omega^2]}, \quad (1)$$

where $g_{eff}^{\uparrow\downarrow}$ is the effective spin-mixing conductance, h is the microwave magnetic field, γ is the gyro-magnetic ratio, M_s is the saturation magnetization, and $\omega = 2\pi f$. θ_M is the out-of-plane angle of the magnetization-precession axis [see Fig. 1(a)]. $A(\theta_M) = 2\omega[4\pi M_s \gamma \sin^2 \theta_M + \sqrt{(4\pi M_s \gamma)^2 \sin^4 \theta_M + 4\omega^2}]^{-1}$ is the precession ellipticity factor. When the magnetization-precession axis is oblique to the film plane, the ISHE voltage V_{ISHE} is proportional to $j_s(\theta_M) \sin \theta_M$ because of $\mathbf{j}_s^{Pt} \parallel \mathbf{j}_c^{Pt} \times \boldsymbol{\sigma}$ [26], where j_s^{Pt} is the spin current density injected into the Pt layer and j_c^{Pt} is the charge current density generated by the ISHE. $\boldsymbol{\sigma}$ is the spin-polarization direction of the spin current, which is parallel to the magnetization-precession axis. As shown in Fig. 2(a), this model well reproduces the experimental data only for $d_{NiO} = 0$ nm (see the solid curve). For the calculation, we determined θ_M and M_s from measured θ_H dependence of H_{res}, shown in Fig. 2(b), by solving $\omega = \gamma \sqrt{H_X H_Y}$, where $\omega = 2\pi f$, $H_X = H_{res} \cos(\theta_H - \theta_M) - M_{eff} \cos^2 \theta_M$, and $H_Y = H_{res} \cos(\theta_H - \theta_M) - M_{eff} \cos(2\theta_M)$ [27–31] [see the inset to Figs. 2(b) and 2(c)]. $M_{eff} \simeq M_s$ is the effective demagnetization field.

To clarify the origin of the anomaly in the θ_H dependence of V_{ISHE} for the $Ni_{81}Fe_{19}$/NiO/Pt trilayers with $d_{NiO} \neq 0$ nm, we plot θ_M dependence of V_{ISHE} in Fig. 2(c). Since $j_c^{Pt}(\theta_M)$ does not change drastically with θ_M, V_{ISHE} is approximately proportional to $\sin \theta_M$. In fact, the θ_M dependence of V_{ISHE} is consistent with this scenario for the $Ni_{81}Fe_{19}$/Pt bilayer ($d_{NiO} = 0$ nm). However, for the $Ni_{81}Fe_{19}$/NiO/Pt trilayers, the measured V_{ISHE} values are proportional to $\sin \theta_M$ only at $|\theta_M| < 45°$ as shown in Fig. 2(c); V_{ISHE} deviates from $\sin \theta_M$ at $|\theta_M| > 45°$ with increasing the thickness of the NiO layer.

The drastic change in V_{ISHE} at $|\theta_M| > 45°$ indicates that the nontrivial variation of V_{ISHE} is caused by two-magnon scattering in the $Ni_{81}Fe_{19}$/NiO/Pt trilayers. The two-magnon scattering can be induced only when $|\theta_M| > 45°$ because the degenerated states with $k = 0$ mode disappear at $|\theta_M| < 45°$
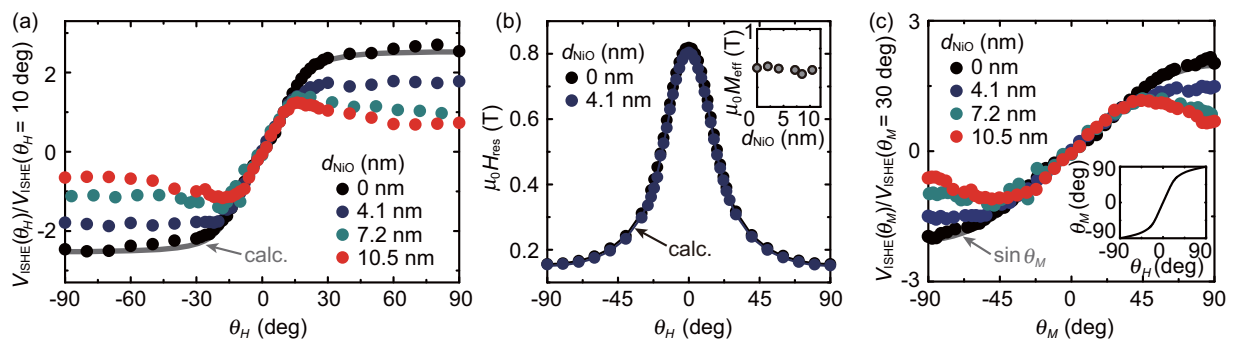

FIG. 2. (a) Out-of-plane magnetic field angle θ_H dependence of the ISHE voltage V_{ISHE} for the $Ni_{81}Fe_{19}$/NiO/Pt trilayers with $d_{NiO} = 0$, 4.1, 7.2, and 10.5 nm. The solid curve is the theoretical prediction based on the model of the spin pumping and ISHE, $j_s(\theta_M) \sin \theta_M$. (b) θ_H dependence of the FMR field H_{res} for $d_{NiO} = 0$ and 4.1 nm. The solid curves are the fitting results. The inset sows the d_{NiO} dependence of the effective demagnetization field M_{eff}. (c) Out-of-plane angle of the magnetization-precession axis, θ_M, dependence of V_{ISHE} for the $Ni_{81}Fe_{19}$/NiO/Pt trilayers. The solid curve is a function proportional to $\sin \theta_M$. The inset shows θ_H dependence of θ_M for $d_{NiO} = 0$.

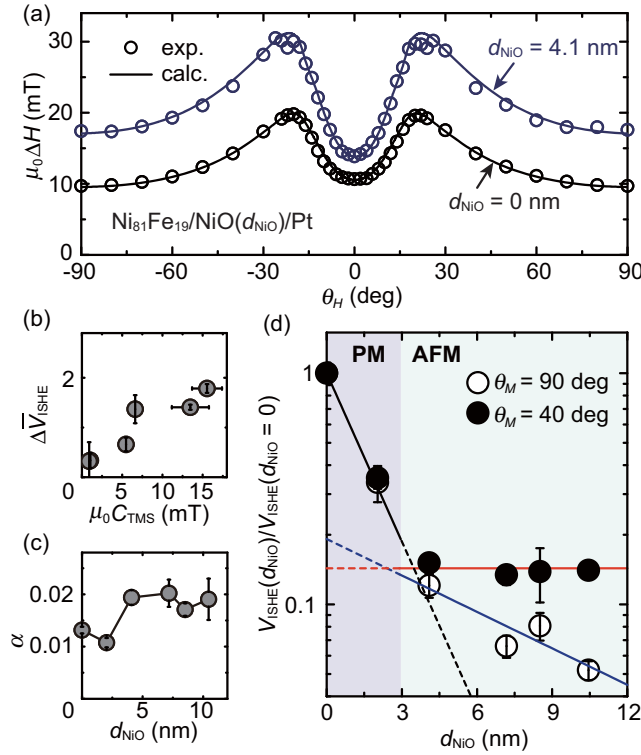FIG. 3. (a) θ_H dependence of the peak-to-peak FMR linewidth ΔH for $d_{NiO} = 0$ nm and 4.1 nm. The open circles are the experimental data and the solid curves are the fitting results [23]. (b) The relation between the amplitude of the two-magnon scattering C_{TMS} and $\Delta \bar{V}_{ISHE} \equiv V_{ISHE}^{calc}(\theta_H = 90°)/V_{ISHE}^{calc}(\theta_H = 10°) - V_{ISHE}^{exp}(\theta_H = 90°)/V_{ISHE}^{exp}(\theta_H = 10°)$, where $V_{ISHE}^{calc(exp)}(\theta_H)$ is the calculated(measured) ISHE voltage at θ_H. (c) d_{NiO} dependence of the magnetic damping constant α. (d) d_{NiO} dependence of V_{ISHE} at $\theta_M = 90°$ (open circles) and $40°$ (solid circles). The solid line in black is the fitting result using an exponential function, $\exp(-d_{NiO}/\lambda_{NiO})$, for $d_{NiO} < 3$ nm. The solid lines in blue and red are the fitting result for the data at $\theta_M = 90°$ and $\theta_M = 40°$ for $d_{NiO} > 3$ nm, respectively.

[30–32]. Here, as shown in Fig. 1(b), the peak-to-peak FMR linewidth ΔH is clearly enhanced by inserting the NiO layer, despite the negligible change in the effective demagnetization field M_{eff} [see the inset to Fig. 2(b)]. To quantitatively study the damping enhancement induced by the NiO insertion, we plot θ_H dependence of ΔH in Fig. 3(a). Figure 3(a) shows $\Delta H(\theta_H = \theta_M = 0°) \simeq \Delta H(\theta_H = \theta_M = 90°)$ for $d_{NiO} = 0$ nm, while $\Delta H(\theta_H = \theta_M = 0°) < \Delta H(\theta_H = \theta_M = 90°)$ for $d_{NiO} = 4.1$ nm. This result indicates that $\Delta H(\theta_H = 90°)$ for the $Ni_{81}Fe_{19}/NiO/Pt$ trilayer is influenced by the two-magnon scattering. In fact, the measured θ_H dependence of ΔH is well reproduced by a calculation which takes into account the additional damping due to the two-magnon scattering as shown in Fig. 3(a) [28,33] (for details, see Ref. [23]). To clarify the relation between the amplitude of the two-magnon scattering C_{TMS} and the voltage suppression, we characterize the suppression of V_{ISHE} induced by the NiO insertion as the difference between the measured V_{ISHE} and V_{ISHE} calculated using the conventional spin-pumping model, $\Delta \bar{V}_{ISHE} \equiv V_{ISHE}^{calc}(\theta_H = 90°)/V_{ISHE}^{calc}(\theta_H = 10°) - V_{ISHE}^{exp}(\theta_H = 90°)/V_{ISHE}^{exp}(\theta_H = 10°)$, where $V_{ISHE}^{calc}(\theta_H)$ and $V_{ISHE}^{exp}(\theta_H)$ are

the calculated and measured ISHE voltage at θ_H, respectively [see Fig. 2(a)]. In Fig. 3(b), we plot $\Delta \bar{V}_{ISHE}$ with respect to C_{TMS}, extracted by the calculation shown in Fig. 3(a). As shown in Fig. 3(b), $\Delta \bar{V}_{ISHE}$ increases with C_{TMS}, supporting that the suppressed V_{ISHE} signals at $|\theta_M| > 45°$ is caused by the two-magnon scattering.

The two-magnon scattering in the $Ni_{81}Fe_{19}/NiO/Pt$ trilayers is caused by a random fluctuation of the exchange bias, which is inevitable in ferromagnetic/antiferromagnetic junctions. The two-magnon scattering is known to be activated by the random fluctuation of uniaxial anisotropy, surface/interface roughness, and defects [28–31,34]. Here, we found that the surface roughness of the NiO layer is almost unchanged with d_{NiO} [23], showing that the two-magnon scattering cannot be attributed to the roughness effect because the two-magnon scattering increases with d_{NiO} in the $Ni_{81}Fe_{19}/NiO/Pt$ trilayer [see Fig. 2(c)]. We note that in the $Ni_{81}Fe_{19}/NiO/Pt$ trilayers, the NiO layer is polycrystalline, as evidenced by the x-ray diffractometry [23]. This suggests that the two-magnon scattering is induced by the random fluctuation of uniaxial anisotropy due to randomly oriented exchange bias fields, which is caused by statistical distribution of antiferromagnetic grains in the polycrystalline NiO layer [33]. The random fluctuation of uniaxial anisotropy due to the randomly oriented exchange bias increases with d_{NiO} [33], and thus the amplitude of the two-magnon scattering C_{TMS} increases with d_{NiO}, which is consistent with the enhancement of the two-magnon scattering by increasing d_{NiO} in the $Ni_{81}Fe_{19}/NiO/Pt$ device.

From the calculation of the θ_H dependence of ΔH, we also extracted the damping constant $\alpha = \mu_0[\Delta H - (\Delta H_{inhomo} + \Delta H_{TMS})](\sqrt{3}/2)(\gamma \Xi/\omega)$, where ΔH_{inhomo} and ΔH_{TMS} are the linewidth due to inhomogeneity and two-magnon scattering, respectively. Ξ is the dragging function [23]. Figure 3(c) shows that α decreases at $d_{NiO} = 2.0$ nm, while α increases above $d_{NiO} = 4.1$ nm, consistent with previous reports [10,12]; α decreases due to the decoupling of the $Ni_{81}Fe_{19}$ and Pt layers by the insulating and non-Néel-ordered NiO layer because the Néel temperature of 2-nm-thick NiO is below the room temperature [35–37]. Above $d_{NiO} = 4.1$ nm, α increases because of the enhanced antiferromagnetic correlation due to the thickness growth [10,38].

Commonly, the spin decay length λ_{NiO} of NiO is obtained from the thickness d_{NiO} dependence of V_{ISHE} at $\theta_H = \theta_M = 90°$ [10–12]. Following this procedure, we plot the d_{NiO} dependence of V_{ISHE} at $\theta_M = 90°$ in Fig. 3(d). This result shows that the spin decay length is increased from $\lambda_{NiO} = 1.9$ nm for $d_{NiO} < 3$ nm to $\lambda_{NiO} = 7.9 \pm 2.3$ nm for $d_{NiO} > 3$ nm. The increase of λ_{NiO} can be attributed to the paramagnetic to antiferromagnetic transition; for $d_{NiO} < 3$ nm, the Néel temperature is lower than the room temperature, while the NiO layer with $d_{NiO} > 3$ nm is antiferromagnetic at room temperature [10,35,36]. $\lambda_{NiO} \simeq 8$ nm in the antiferromagnetic state is consistent with previous reports [10,12]. However, we note that, as is clear from Fig. 2(a), the V_{ISHE} signals at $\theta_H = 90°$ are strongly suppressed by the two-magnon scattering. This results in underestimation of the spin decay length in the antiferromagnetic state because the voltage suppression increases with d_{NiO}.
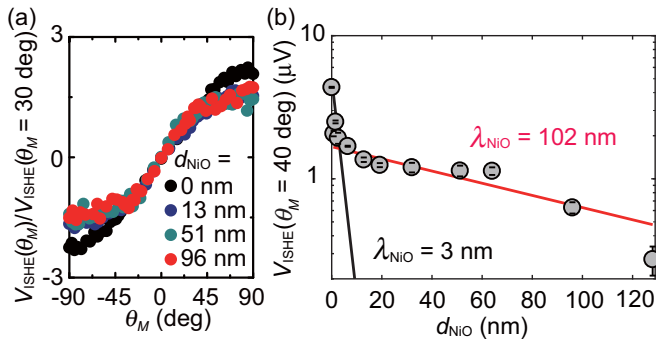
FIG. 4. (a) θ_M dependence of V_{ISHE} for the $\text{Ni}_{81}\text{Fe}_{19}/\text{NiO/Pt}$ trilayers with $d_{\text{NiO}} = 0$, 13, 51, and 96 nm. (b) d_{NiO} dependence of V_{ISHE} at $\theta_M = 40°$. The solid line in black is the fitting result using an exponential function, $\exp(-d_{\text{NiO}}/\lambda_{\text{NiO}})$, for $d_{\text{NiO}} < 2$ nm. The solid line in red is the fitting result for $d_{\text{NiO}} > 6$ nm.

The intrinsic spin decay length, where the two-magnon contribution is excluded, can be determined only from the d_{NiO} dependence of V_{ISHE} at $|\theta_M| < 45°$, where the voltage suppression due to the two-magnon scattering is absent. As shown in Fig. 3(d), the d_{NiO} dependence of V_{ISHE} at $\theta_M = 40°$ is clearly different from that at $\theta_M = 90°$; at $\theta_M = 40°$, V_{ISHE} is almost independent of d_{NiO}, indicating that λ_{NiO} is much larger than 10 nm.

To quantify the intrinsic spin decay length in NiO, we measured the θ_H dependence of V_{ISHE} for $\text{Ni}_{81}\text{Fe}_{19}/\text{NiO/Pt}$ devices with large d_{NiO}, as shown in Fig. 4(a). The devices are a different batch from those used to obtain the data shown in Figs. 1–3. The NiO layer is composed of dense columns with in-plane size of around 20 nm as confirmed by transmission electron microscopy (TEM) and atomic force microscopy [23]. Figure 4(a) shows that V_{ISHE} is suppressed by the two-magnon scattering, although the two-magnon effect is weaker than that in Fig. 2(c). This result also shows that V_{ISHE} can be observed even for $d_{\text{NiO}} = 128$ nm. We have checked the insulating property of the NiO layer and found that the resistance of the NiO layer is high enough to electrically separate the Pt

and $\text{Ni}_{81}\text{Fe}_{19}$ layers [23]. Thus the measured signals can only be attributed to the ISHE voltage generated in the Pt layer.

In Fig. 4(b), we plot the d_{NiO} dependence of V_{ISHE} at $\theta_M = 40°$. This result shows that the intrinsic spin decay length of the polycrystalline NiO layer in the antiferromagnetic state is $\lambda_{\text{NiO}} = 102 \pm 32$ nm, which is almost ten times longer than previously reported values [10,12]. This result shows that the characteristic length of spin decay in NiO changes by two-orders of magnitude through the paramagnetic to antiferromagnetic transition, illustrating the crucial role of the antiferromagnetic order for efficient spin transport in antiferromagnetic insulators.

IV. CONCLUSIONS

In summary, we investigated magnonic spin transport in an antiferromagnetic insulator NiO. We found that in the in-plane magnetic field geometry, the spin transport signal is strongly suppressed by the two-magnon scattering. Our result shows that the intrinsic spin decay length of polycrystalline NiO with columnar structure is around 100 nm, which is an order of magnitude longer than that previously believed. We note that the two-magnon scattering at the $\text{Ni}_{81}\text{Fe}_{19}/\text{NiO}$ interface arises from the randomly oriented exchange bias fields, which is inevitable in ferromagnet/antiferromagnet junctions. This indicates that the effect from the two-magnon scattering is ubiquitous in antiferromagnetic spin-transport studies via various techniques including the spin Seebeck and spin pumping. As long as a ferromagnet is used as a spin current injector, the two-magnon scattering masks the intrinsic spin transport properties in antiferromagnets.

[1] I. Žutić, J. Fabian, and S. Das Sarma, Rev. Mod. Phys. **76**, 323 (2004).

[2] *Concepts in Spin Electronics*, edited by S. Maekawa (Oxford University Press, Oxford, 2006).

[3] *Spin Current*, edited by S. Maekawa, S. O. Valenzuela, E. Saitoh, and T. Kimura (Oxford University Press, Oxford, 2012).

[4] Y. Kajiwara, K. Harii, S. Takahashi, J. Ohe, K. Uchida, M. Mizuguchi, H. Umezawa, H. Kawai, K. Ando, K. Takanashi, S. Maekawa, and E. Saitoh, Nature (London) **464**, 262 (2010).

[5] L. Cornelissen, J. Liu, R. Duine, J. B. Youssef, and B. Van Wees, Nat. Phys. **11**, 1022 (2015).

[6] D. Wesenberg, T. Liu, D. Balzar, M. Wu, and B. L. Zink, Nat. Phys. **13**, 987 (2017).

[7] T. Jungwirth, X. Marti, P. Wadley, and J. Wunderlich, Nat. Nanotechnol. **11**, 231 (2016).

[8] M. B. Jungfleisch, W. Zhang, and A. Hoffmann, Phys. Lett. A **382**, 865 (2018).

[9] V. Baltz, A. Manchon, M. Tsoi, T. Moriyama, T. Ono, and Y. Tserkovnyak, Rev. Mod. Phys. **90**, 015005 (2018).

[10] H. Wang, C. Du, P. C. Hammel, and F. Yang, Phys. Rev. Lett. **113**, 097202 (2014).

[11] C. Hahn, G. De Loubens, V. V. Naletov, J. B. Youssef, O. Klein, and M. Viret, Europhys. Lett. **108**, 57005 (2014).

[12] H. Wang, C. Du, P. C. Hammel, and F. Yang, Phys. Rev. B **91**, 220410(R) (2015).

[13] T. Moriyama, S. Takei, M. Nagata, Y. Yoshimura, N. Matsuzaki, T. Terashima, Y. Tserkovnyak, and T. Ono, Appl. Phys. Lett. **106**, 162406 (2015).

[14] S. Takei, T. Moriyama, T. Ono, and Y. Tserkovnyak, Phys. Rev. B **92**, 020409(R) (2015).

[15] S. Seki, T. Ideue, M. Kubota, Y. Kozuka, R. Takagi, M. Nakamura, Y. Kaneko, M. Kawasaki, and Y. Tokura, Phys. Rev. Lett. **115**, 266601 (2015).

[16] W. Lin, K. Chen, S. Zhang, and C. L. Chien, Phys. Rev. Lett. **116**, 186601 (2016).

[17] S. Takei, B. I. Halperin, A. Yacoby, and Y. Tserkovnyak, Phys. Rev. B **90**, 094408 (2014).

[18] S. M. Rezende, R. L. Rodríguez-Suárez, and A. Azevedo, Phys. Rev. B **93**, 054412 (2016).

[19] S. A. Bender, H. Skarsvåg, A. Brataas, and R. A. Duine, Phys. Rev. Lett. **119**, 056804 (2017).

[20] A. Qaiumzadeh, H. Skarsvåg, C. Holmqvist, and A. Brataas, Phys. Rev. Lett. **118**, 137201 (2017).

[21] R. Lebrun, A. Ross, S. Bender, A. Qaiumzadeh, L. Baldrati, J. Cramer, A. Brataas, R. Duine, and M. Kläui, Nature (London) **561**, 222 (2018).

[22] W. Yuan, Q. Zhu, T. Su, Y. Yao, W. Xing, Y. Chen, Y. Ma, X. Lin, J. Shi, R. Shindou *et al.*, Sci. Adv. **4**, eaat1098 (2018).

[23] See Supplemental Material at http://link.aps.org/supplemental/10.1103/PhysRevResearch.1.013013 for a detailed description of sample fabrication and characterization and evaluation of two-magnon scattering amplitude.

[24] Y. Tserkovnyak, A. Brataas, and G. E. W. Bauer, Phys. Rev. B **66**, 224403 (2002).

[25] E. Saitoh, M. Ueda, H. Miyajima, and G. Tatara, Appl. Phys. Lett. **88**, 182509 (2006).

[26] K. Ando, S. Takahashi, J. Ieda, Y. Kajiwara, H. Nakayama, T. Yoshino, K. Harii, Y. Fujikawa, M. Matsuo, S. Maekawa, and E. Saitoh, J. Appl. Phys. **109**, 103913 (2011).

[27] S. Mizukami, Y. Ando, and T. Miyazaki, Phys. Rev. B **66**, 104413 (2002).

[28] J. Lindner, I. Barsukov, C. Raeder, C. Hassel, O. Posth, R. Meckenstock, P. Landeros, and D. L. Mills, Phys. Rev. B **80**, 224421 (2009).

[29] P. Landeros, R. E. Arias, and D. L. Mills, Phys. Rev. B **77**, 214405 (2008).

[30] R. Arias and D. L. Mills, Phys. Rev. B **60**, 7395 (1999).

[31] R. Arias and D. Mills, J. Appl. Phys. **87**, 5455 (2000).

[32] H. Kurebayashi, T. Skinner, K. Khazen, K. Olejník, D. Fang, C. Ciccarelli, R. Campion, B. Gallagher, L. Fleet, A. Hirohata *et al.*, Appl. Phys. Lett. **102**, 062415 (2013).

[33] H. Sakimura, A. Asami, T. Harumoto, Y. Nakamura, J. Shi, and K. Ando, Phys. Rev. B **98**, 144406 (2018).

[34] A. Azevedo, A. B. Oliveira, F. M. De Aguiar, and S. M. Rezende, Phys. Rev. B **62**, 5331 (2000).

[35] M. Gruyters, J. Magn. Magn. Mater. **248**, 248 (2002).

[36] A. Baruth and S. Adenwalla, Phys. Rev. B **78**, 174407 (2008).

[37] X. Wang, C. O. Pauyac, and A. Manchon, Phys. Rev. B **89**, 054405 (2014).

[38] X. Lang, W. Zheng, and Q. Jiang, Nanotechnology **18**, 155701 (2007).